Chemical Engineering Journal Advances 26 (2026) 101137

Contents lists available at ScienceDirect

Chemical Engineering Journal Advances

journal homepage: www.sciencedirect.com/journal/chemical-engineering-journal-advances

Isopropylation of naphthalene by silica–alumina catalysts: coordination of active species determines the selectivity

Sang–Ho Chung [a,b,1,*], José Nuno Almeida [c,1], Federico Gubellini [a], Raghda Makarem [c], Javier Ruiz–Martínez [c], N. Raveendran Shiju [a,*]

[a] Catalysis Engineering Group, Van 't Hoff Institute for Molecular Sciences, University of Amsterdam, 1090 GD Amsterdam, The Netherlands
[b] School of Energy and Chemical Engineering, Ulsan National Institute of Science and Technology (UNIST), Ulsan 44919, Republic of Korea
[c] KAUST Catalysis Center (KCC), King Abdullah University of Science and Technology, Thuwal 23955, Saudi Arabia

ARTICLE INFO

Keywords:
Naphthalene
Alkylation
Solid acid catalysts
Amorphous silica–alumina
Solid-state nuclear magnetic resonance spectroscopy

ABSTRACT

Tailoring the local coordination environment of acid sites in amorphous silica-alumina (ASA) catalysts remains a critical challenge for controlling reactivity and product selectivity in the isopropylation of naphthalene. Here, we demonstrate that a systematic co-precipitation strategy, specifically controlling the precursor-mixing phase and the pH-adjustment sequence, profoundly dictates the specific surface area and macroscopic acid-site distribution of ASA catalysts. By correlating these macroscopic properties with atomic-scale insights from advanced 2D ^{27}Al Double Quantum-Single Quantum (DQ-SQ) MAS NMR, we reveal that direct mixing of Si and Al precursors at pH 8.7 selectively creates proximate Al(IV)–Al(V) pairs. We identify that these proximate pairs are closely associated with the strong acidity and the resulting performance enhancement. However, this strongly acidic environment promotes extensive over-alkylation into tri- and tetra-isopropylnaphthalene (PIPN). Conversely, when mixing is performed and the pH is subsequently adjusted to 9.7, it yields an ASA catalyst with a unique structural motif characterized by two proximal, distinct Al(VI) centers. This catalyst features a higher density of weak acid sites, which effectively suppresses over-alkylation to favor di-isopropylnaphthalene. These findings provide a clear link between macroscopic synthesis conditions and the atomic-level structural motifs of acid sites, enabling the rational design of ASA catalysts for targeted aromatic alkylation.

1. Introduction

Alkylated naphthalenes find their applications in multiple industries [1,2]. Among the alkylated naphthalenes, 2,6-di-isopropylnaphthalene (2,6-DIPN) plays a pivotal role in the food industry as a plant growth regulator, as well as in advanced polymer applications [1,3–8]. For example, polyethylene naphthalate (PEN) is a high performance thermoplastic polyester, showing its greater mechanochemical properties compared to polyethylene terephthalate (PET), such as higher glass transition temperature (122°C and 80°C for PEN and PET, respectively), higher Young's modulus (5200 MPa and 3900 MPa), lower oxygen permeability (20 and 56 cm^3 m^{-2} day^{-1} atm^{-1}), and lower thermal shrinkage (0.6 % and 1.3 %) [6–8]. The market estimates the growing demand of PEN as 4000–7000 tons per year as packaging materials and flexible film in electronics [6,7].

Industrially, DIPN is produced by Rütgers Kureha Solvents process, using liquid-phase naphthalene and gas-phase propylene over an amorphous silica–alumina catalyst (Fig. 1a) [9,10]. The isopropylation of naphthalene initiates with the formation of propylene carbocation over acid catalysts [11]. The carbocation can then attack naphthalene at the α-positions (1,4,5 and 8 on the naphthalene double ring) or the β-positions (2,3,6 and 7 on the naphthalene double ring) (Fig. 1b). The α-isopropyl naphthalene is kinetically preferred, resulting from an electrophilic substitution of the alkylating agent at the electron-rich α-position of naphthalene [12–14]. The β-isopropyl naphthalene can be formed with a more stable secondary carbocation at the β-position of the ring [11]. Given the thermodynamic preference for DIPN products, particularly 2,6- and 2,7-DIPN, the industrial-scale isopropylation of naphthalene is executed in four consecutive reactors, and this process involves longer reaction times and higher reaction temperatures to favor the desired DIPN isomers (Fig. 1a) [11,14]. Additionally, to maximize DIPN yield, the mixture of unreacted naphthalene and

---

* Corresponding authors.
E-mail addresses: s.chung@unist.ac.kr (S. Chung), n.r.shiju@uva.nl (N.R. Shiju).

[1] These authors contributed equally.

https://doi.org/10.1016/j.ceja.2026.101137

mono-isopropylnaphthalene (MIPN) is recycled back to the alkylation reactors, while the heavier PIPN products undergo trans-alkylation in separate reactors. The resulting mixture is then subjected to three vacuum distillation columns to separate fractions, including unreacted naphthalene, MIPN, DIPN, and tri- and tetra-isopropylnaphthalene (PIPN) (Fig. 1a).

Meanwhile, H-Mordenite zeolite (MOR) has been extensively studied in the literature due to its shape-selective catalysis during naphthalene isopropylation [12,14–27]. The restricted pore structures within the MOR zeolite channels induce steric hindrance to the transition states during DIPN formation, and consequently, the variation in diffusion rates between 2,6- and 2,7-DIPN leads to the selective formation of 2,6-DIPN [17,23]. Despite the advantages of zeolites, the resulting products remain complex mixtures containing MIPN, various DIPN isomers (including the thermodynamically dominant 2,7-DIPN), and PIPN, all of which require extensive fine separation by distillation, crystallization, or adsorption to achieve high purity [28] In this sense, amorphous silica-alumina could provide a more "open" framework that achieves high activity, using tailored aluminum coordination to prevent the formation of heavy byproducts.

In this study, a series of amorphous silica–alumina catalysts were prepared for naphthalene isopropylation, and their catalytic performances were tested under conditions resembling the industrial process with gaseous propylene. We also compared the catalytic performance of

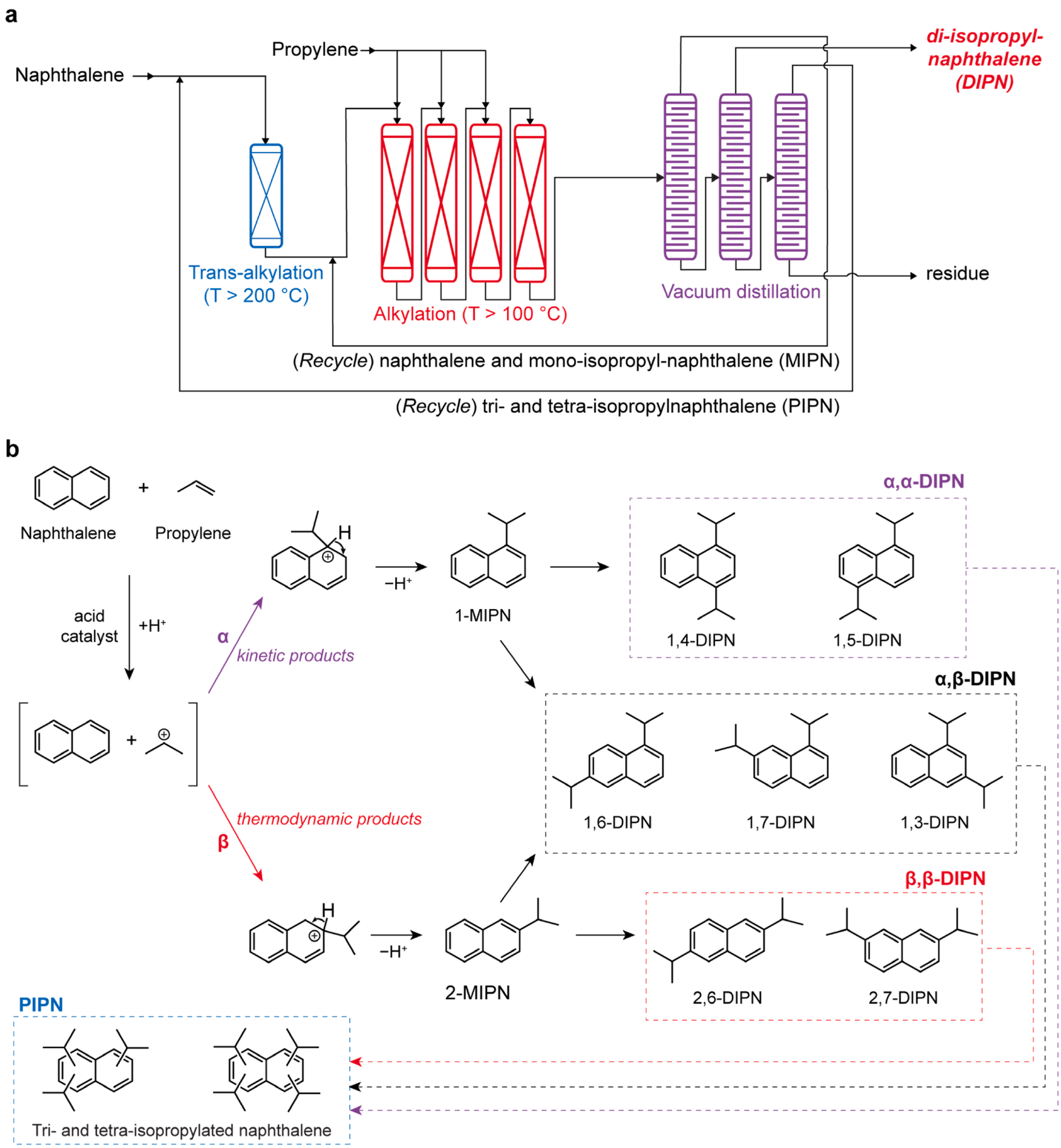

Fig. 1. (a) Reactor scheme for the industrial naphthalene isopropylation. (b) The reaction pathways of naphthalene isopropylation via carbocation formation over an acid catalyst.

the prepared amorphous silica–alumina catalysts with that of zeolite-based catalysts. The amorphous silica–alumina catalysts were characterized by multiple techniques such as *n*-butylamine titration, X-ray diffraction, nitrogen physisorption, and solid-state nuclear magnetic resonance (NMR) spectroscopy. Our results highlight that the coordination of aluminum species in amorphous silica–alumina catalysts, influenced during the coprecipitation of silica and alumina precursors, significantly impacts the catalytic performance in naphthalene isopropylation.

2. Experimental

2.1. Materials

The chemicals such as sodium water glass (SiO_2 26.5 %), sodium aluminate (Al_2O_3 53 %), HNO_3 (70 %), NH_4NO_3 (98 %), NaOH (98 %), *n*-butylamine (99.5 %), acetonitrile (99.8 %), naphthalene (99 %), decalin (mixture of *cis* and *trans*, 99 %), ethanol (99.5 %), acetone (99.5 %), toluene (99.8 %), 1-methyl naphthalene (99.5 %) were purchased from Sigma Aldrich and used without further purification. Mordenite catalysts in the protonic form such as H-MOR (silicon-to-aluminum ratio (SAR) = 15, Tosoh) and H-MOR (SAR = 40, Sud Chemie) were provided by University of Bologna, Italy (F. Cavani group). NH_4-ZSM-5 (SAR = 50) and H-Y (SAR = 5.1) were purchased from Zeolyst.

2.2. Catalyst preparation

Four amorphous silica–alumina catalysts were prepared by co-precipitation [29], by changing the mixing phases and the final pH of the mixture solution (Fig. 2a). Two aqueous solutions of sodium water glass and sodium aluminate in a total volume of 100 mL, were separately prepared as silicon and aluminum precursors, respectively, to obtain the amorphous silica–alumina catalysts with the silicon-to-aluminum ratio of 6 (SAR 6). ASA1 and ASA3 samples were prepared by direct mixing of the two precursors (mixing phase 1). It should be noted that the fast gelation occurred during the direct mixing of the silicon and aluminum precursors, resulting in a considerably thick mixture. Meanwhile, the viscosity of the gel can be greatly reduced by adding silicon and aluminum precursors to the DI water (mixing phase 2), and the two additional mixture gels were prepared. The pH of the mixture gel was adjusted to 8.7 or 9.7, adding 0.5 M HNO_3 solution dropwise. To obtain the homogenous mixture, the solutions were mixed with vigorous stirring using a drill mixer for 24 h. The precipitants were filtered and ion-exchanged with 0.5 M NH_4NO_3 three times (8 h per exchange), using a tube roller mixer. After ion-exchange, the mixture was finally treated with DI water using a tube roller mixer for 2 h. After filtration, the resulting solids were thoroughly rinsed with DI water, dried at 120°C for 15 h, and calcined at 550 °C for 5 h with a heating ramp of 2.5 °C min^{-1}.

Commercial ZSM-5 (NH_4 form) was converted into proton form (H-ZSM-5) by calcination at 550 °C for 5 h in a static oven (heating ramp of 2.0 °C min^{-1}). The H-ZSM-5 samples were post-treated by desilication in aqueous NaOH solutions at different concentrations (0.1 or 0.5 M, 30 mL per gram of zeolite) [30]. The desilication was performed at 65 °C and the suspensions were quenched in an ice-bath after 30 min. The resulting solids were filtered, washed thoroughly with DI water, and dried at 120 °C for 15 h. The desilicated samples were then converted into the NH_4 form by ion-exchange in 0.1 M aqueous NH_4NO_3 solution (100 mL per gram of zeolite) at 23 °C for 12 h. After three consecutive ion-exchange treatments, the proton form of desilicated zeolites was obtained by calcination at 550 °C for 5 h in a static oven (heating ramp of 2.0 °C min^{-1}).

2.3. Characterization

Powder XRD patterns of the catalysts were recorded with Ni-filtered Cu Kα radiation (λ = 1.54 Å) on a Rigaku Miniflex II. X-ray

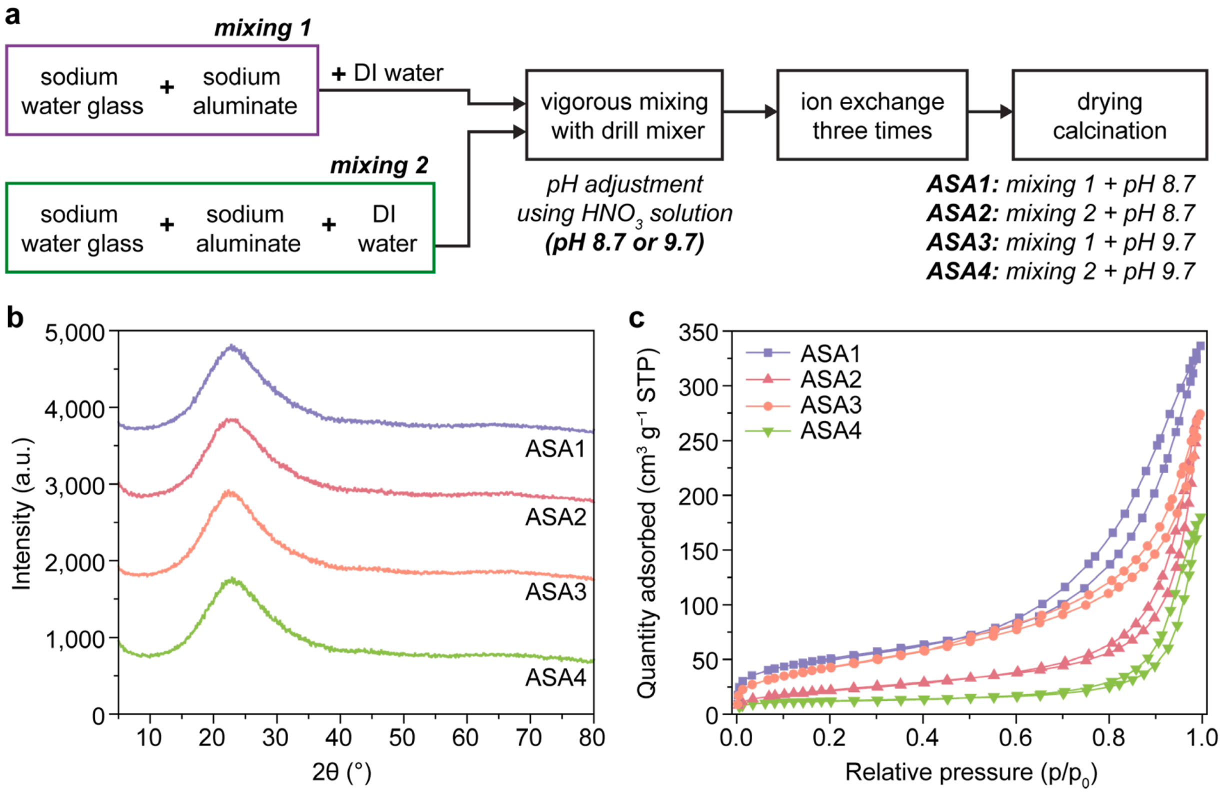

Fig. 2. (a) Preparation methods, (b) Powder X-ray diffraction (PXRD) patterns, and (c) N_2 isotherms for amorphous silica–alumina. The PXRD patterns are offset for clarity.

diffractometer was equipped with a secondary curved graphite-crystal monochromator. The samples were analyzed in the 2θ range of 5 to 80° with a scan rate of 0.05° s^{-1}.

The acidity and the number of acidic sites of the catalysts were measured by a potentiometric titration method [31]. A suspension of the calcined powder catalyst in acetonitrile was titrated with 0.05 *n*-butylamine/acetonitrile solution at a flow rate of 0.05 mL min^{-1} [32,33]. The variation of electric potential during the titration was measured with a digital pH meter (Eutech Instruments, PC2700) equipped with a standard calomel electrode.

Pyridine adsorption FTIR was performed in a Nicolet 6700 spectrometer using a lower spectral cutoff mercury cadmium telluride (MCT-B) detector. A self-pressed pellet of each ASA sample was prepared using approximately 15–20 mg of sample. The pellet was then dehydrated under 10^{-6} mbar vacuum at 450°C for 3 h. After this, three pulses of pyridine at its vapor pressure under ambient conditions were introduced. After saturation, excess pyridine was removed by evacuation at 150 °C for 1 h. All spectra were collected in the 1000–5000 cm^{-1} range at a resolution of 4 cm^{-1} and with 64 scans co-added. The concentrations of Brønsted (BAS) and Lewis (LAS) acid sites were determined from the integrated areas under the maxima at 1545 and 1456 cm^{-1}, using extinction coefficients of 1.67 and 2.22 cm^{-1}, respectively [34].

Transmission Electron Microscopy (TEM) was employed to investigate the morphological properties of the commercial and desilicated ZSM-5. The TEM analysis was conducted using a Thermo Fisher Scientific Talos F200X G2 microscope, equipped with a high-brightness Schottky field emission gun. The measurements were performed at an accelerating voltage of 200 kV with a probe current of 10 nA. The instrument provided a spatial resolution of 1.2 Å, and TEM images were acquired using a Ceta CMOS camera.

Nitrogen physisorption was measured at –196 °C using a Micromeritics ASAP 2420 high-throughput analysis system. Samples were outgassed at 300 °C under vacuum for 8 h. The specific surface areas were estimated according to the Brunauer-Emmett-Teller (BET) method in the relative pressure range (p/p_0) of 0.05–0.25.

^{29}Si magic angle spinning (MAS) nuclear magnetic resonance (NMR) experiments were performed on a Bruker 900 MHz (21.1 T) wide-bore magnet with an AVANCE-III console equipped with a Bruker 3.2 mm HXY MAS probe. Samples for the solid-state NMR experiments were ground and transferred to a 3.2 mm zirconia rotor. ^{29}Si π/2 pulses were applied with a field strength of 125 kHz, a 20 s recycle delay and an accumulation of 128 scans. ^{27}Al MAS NMR experiments were performed on a Bruker 600 MHz (14.1 T) wide-bore magnet with an AVANCE-III console. The one-dimensional (1D) ^{27}Al direct excitation spectrum was recorded with accumulations of 2048 scans, using a ^{27}Al π/6 hard pulse with a field strength of 170 kHz and 0.5 s recycle delay. The two-dimensional (2D) ^{27}Al *z*-filtered triple quantum (3Q) MAS NMR spectra were recorded using a 0.5 s recycle delay with 7200 scans with 50 μs t1 (where t1 denotes time-domain increments). The optimized pulse widths for excitation, conversion and central-transition selective pulses were 3.7, 1.1 and 20 μs, respectively. The z-filter delay between the conversion and the selective pulse was 20 μs. Before Fourier transformation, the 1D and 2D NMR spectra were processed using an exponential window and a π/3-shifted squared sine-bell window in the F1 dimension, respectively. The 3Q MAS data were processed with a shearing transformation available in Bruker Topspin software (v3.6.3). The isotropic shift (δ_{iso}), the quadrupole products (P_Q) and the quadrupolar coupling constant (C_{QCC}) were determined by the center of the gravity of the projected resonances along the isotropic and anisotropic dimensions from the sheared 3Q MAS spectra ($\delta_{iso} = (17\delta_{F1} + 10\delta_{F2})/27$ and $P_Q = C_{QCC}\,(1 + \eta^2/3)^{0.5} = \nu_0\,[(8500/81)(\delta_{F1} - \delta_{F2})]^{0.5} \times 10^{-3}$), where the asymmetry parameter of the electric field gradient tensor (η) was set to be 0.5 [35–37]. 2D ^{27}Al–^{27}Al double-quantum single-quantum (DQ–SQ) spectra were recorded using four cycles of BR2_2^1 recoupling sequence to reintroduce the dipolar interactions [38]. The excitation and reconversion periods were 400 μs and the amplitude of radio frequency applied during the BR2_2^1 sequence was 8.7 kHz, which corresponds to a nutation frequency of 13 kHz for the central transition of ^{27}Al. The 2D DQ–SQ spectra were acquired with 8192 scans with the recycle delay of 0.1 s and the phase-sensitive detection was performed using the states-TPPI method. The experiments were performed at room temperature with a MAS frequency of 20 kHz. ^{1}H, ^{29}Si, and ^{27}Al chemical shifts were referenced externally to adamantane, hexamethylcyclosiloxane, and 1.0 M aluminum chloride aqueous solution, respectively.

2.4. Activity test

The naphthalene isopropylation with gaseous propylene as the isopropylation source was carried out in a fixed-bed quartz reactor. Saturated solutions of naphthalene in decalin and gaseous propylene were introduced using a syringe pump (Teledyn Isco 100DX) and mass flow controller (Brooks 5850 E-series), respectively. The catalytic evaluations were performed using 1.0 g of catalyst (particle size: 250–425 μm) at a reaction temperature of 150 °C. The molar feed composition was maintained at a ratio of naphthalene:propylene:decalin = 7.6:19.5:72.9, corresponding to specific flow rates of 9.74 mL min^{-1} (naphthalene), 25.00 mL min^{-1} (propylene), and 93.46 mL min^{-1} (decalin), with a total flow rate of 128.20 mL min^{-1}. Furthermore, all catalyst samples underwent standardized drying and calcination procedures before the reaction to ensure consistent catalytic activity and structural integrity.

Then, the sieved catalysts were sandwiched with quartz wool and placed at the middle of the quartz reactor, and the silicon carbide was added above the catalyst bed to achieve uniform profile of the liquid naphthalene feed to the catalyst bed. A control experiment confirmed that the silicon carbide is inactive, and no naphthalene conversion was observed in the absence of the catalyst. The reaction temperature was measured by placing a thermocouple on the catalyst bed. The reaction products were collected in a cold trap and then analyzed by gas chromatography (GC) [9,39]. Before the GC analysis, the liquid samples were diluted in toluene, with a precise quantity of the internal standard (1-methyl naphthalene). The GC analyses were performed with an Agilent Technologies 7820A machine equipped with a CP-Wax 52 CB column and an FID detector, using helium as a carrier gas. This optimized chromatographic method, which has been previously demonstrated in the literature to effectively resolve DIPN isomers [9], provided clear baseline separation and definitive identification of the respective products, specifically including the 2,6- and 2,7-DIPN pair. The naphthalene conversion and product yields were determined using the following equations with the stoichiometric coefficient of a product mixture with known concentration.

$$\text{Conversion} = \frac{\text{converted cocentration of naphthalene (mol)}}{\text{initial concentration of naphthalene (mol)}} \times 100 \tag{1}$$

$$\text{Yield} = \frac{\text{moles of products/stoichiometric coefficient}}{\text{moles of reactant/stoichiometric coefficient}} \times 100 \tag{2}$$

$$\text{Carbon balance} = \frac{\Sigma\text{Yields of naphthalene and reaction products}}{\text{Conversion of naphthalene}} \tag{3}$$

3. Results and discussion

3.1. Synthesis and morphology

Amorphous silica–alumina catalysts can be synthesized using various methods, such as co-precipitation, aluminum grafting, and deposition-precipitation of Si or Al on Al_2O_3 or SiO_2, respectively [40–45]. Among these approaches, co-precipitation is reported to produce a homogeneously dispersed mixture of silicon and aluminum species within the catalyst [29]. The synthesis parameters for amorphous silica–alumina catalysts by co-precipitation include variations in the mixing phase of the two precursor solutions and in the mixture pH [29,42,46]. We synthesized four different amorphous silica–alumina catalysts using co-precipitation, manipulating the mixing phases of precursors and DI water, and adjusting the final pH of the resulting gel mixtures to control the coagulation and hydrolysis rates (Fig. 2a).

Fig. 2b shows the powder XRD patterns of the prepared amorphous silica–alumina catalysts. All samples show a broad peak at around 2θ 15–30° (Fig. 2b), which is a characteristic feature for amorphous silica without long-range ordering [47,48]. The absence of the diffraction patterns related to γ-alumina domains (2θ 36°, 46° and 66°) suggests homogeneous incorporation of aluminum species in the amorphous silicon oxide network as amorphous silica–alumina catalysts [49,50].

We analyzed the textural properties of the prepared amorphous silica–alumina catalyst using nitrogen physisorption (Fig. 2c, Table 1). The catalysts prepared by mixing phase 1 (ASA1 and ASA3) displayed type IV adsorption isotherms with an H3-type loop characteristic of a gel containing mesopores [29,51,52]. The catalysts with mixing phase 2 (ASA2 and ASA4) showed type IV adsorption isotherms with H2b-type hysteresis loops, suggesting large-pore networks in their structure [53]. The textural properties of the prepared amorphous silica-alumina catalysts are summarized in Table 1. Although diluting the precursors in DI water (mixing phase 2) can ease mechanically mixing during the preparation (Fig. 2a), it did not contribute to achieving a higher surface area for amorphous silica–alumina catalysts. The average pore size of these catalysts was also influenced by the variations in the mixing phases. For instance, the mixing phase 1 produced catalysts with pores of approximately 10 nm, while mixing phase 2 yielded larger pores exceeding 20 nm. Meanwhile, the catalysts prepared with a greater quantity of nitric acid (final pH at 8.7, ASA1 and ASA2) exhibited a two-fold increase in specific surface area compared to ASA3 and ASA4, attributed to the intensified hydrolysis processes (Table 1).

3.2. Acidity measurements

3.2.1. Potentiometric titration of n-butylamine

Various gas-phase techniques are commonly used to determine the acidity of catalysts, such as temperature-programmed desorption (TPD) technique to measure the amount of ammonia [54] adsorbed by the acid sites and Fourier Transform Infrared spectroscopy (FTIR) with pyridine as probe molecule [55,56]. However, it has been reported that the acidic properties determined by gas-phase techniques might not necessarily correlate with those in liquid-phase catalytic reactions [29,57]. The industrial-scale isopropylation of naphthalene involves the use of liquid-phase naphthalene and gas-phase propylene over heterogeneous acid catalysts (specifically, amorphous silica–alumina) in trickle-bed reactors (Fig. 1). To characterize the catalyst's acid sites in a manner more relevant to the operational conditions in the industrial DIPN process, we employed the liquid-phase potentiometric titration of *n*-butylamine [31,58] to assess the acidity of the synthesized catalysts (Fig. 3).

In comparison to other zeolites, H-Mordenite (MOR) zeolites exhibited a lower total acid amount due to the restricted accessibility to the acid sites in the 8 membered-ring (8 MR, 2.6 × 5.7 Å) as opposed to the 12 MR channels (6.5 × 7.0 Å). The acid sites located in the 8 MR side-pockets are not accessible to *n*-butylamine, which has a molecular size similar to that of *n*-hexane [59,60]. With the lower aluminum content, the H-MOR catalyst (SAR40) displayed a reduced amount of acid sites compared to H-MOR-15 [61]. The large-pore H-Y zeolite (7.4 Å) showed the highest total amount of acid sites among the prepared catalysts, attributed to its higher aluminum content accessible for *n*-butylamine (Fig. 3).

Similarly, the acid sites in pristine ZSM-5 are accessible to *n*-butylamine (~5.5 Å), indicating a dominant distribution of the strong acid sites. However, given that the kinetic molecular size of naphthalene is

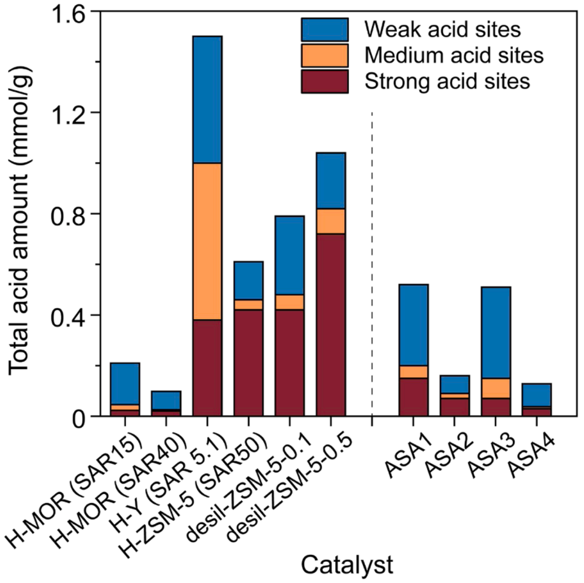

Fig. 3. Acidity of catalysts measured by potentiometric *n*-butylamine titration. The strength of acid sites was categorized by the changes of the electrode potential (E) [58]: $E > 100$ mV (strong acid sites), $100 > E > 0$ mV (medium acid sites), $0 > E > -100$ mV (weak acid sites).

Table 1

Summary of the results of nitrogen physisorption and solid-state 1D ^{27}Al and 2D ^{27}Al MQMAS NMR spectroscopy.

Catalyst	S_{BET} ($m^2\ g^{-1}$)	V_{total} ($cm^3\ g^{-1}$)[a]	V_{micro} ($cm^3\ g^{-1}$)	V_{meso} ($cm^3\ g^{-1}$)	d (nm)[b]	Al(IV): Al(V): Al(VI) ratio (%)[c]	Al species	δ_{iso} (ppm)	C_{QCC} (MHz)
ASA1	179.4	0.52	0.004	0.52	9.8	36: 27: 37	Al(IV)	57.2	1.7
							Al(V)	33.4	4.0
							Al(VI)	8.3	3.3
ASA2	80.6	0.42	-	0.42	20.4	29: 40: 31	Al(IV)	57.7	2.1
							Al(V)	33.9	4.3
							Al(VI)	7.2	4.2
ASA3	155.6	0.43	0.006	0.42	11.6	33: 25: 42	Al(IV)	55.9	1.7
							Al(V)	34.1	4.9
							Al(VI)	6.2, 12.2[d]	3.8, 4.2[d]
ASA4	59.8	0.28	-	0.28	24.8	35: 34: 31	Al(IV)	58.7	2.2
							Al(V)	33.7	4.2
							Al(VI)	6.6	4.2

[a] The total volume of amorphous silica–alumina catalysts were calculated at $p/p_0 = 0.99$.

[b] Pore diameter (d) was calculated using Barrett-Joyner-Halenda (BJH) desorption branch.

[c] The ratio between aluminum species (Al(IV):Al(V):Al(VI)) was calculated after deconvolution, based on 1D ^{27}Al NMR using π/6 hard pulse.

[d] For ASA3 sample, two types of Al(VI) species were observed and denoted in Fig. 5d

approximately 6.5 Å, it implies that naphthalene and alkylated naphthalenes cannot penetrate the ZSM-5 pores [62–65]. To address this limitation, we employed desilication as a post-treatment to modify the ZSM-5 pore structure, aiming for hierarchical pore structures [66,67]. TEM images of the desilicated ZSM-5 sample (0.5 M aqueous NaOH solution, 30 min) exhibit pronounced internal contrast heterogeneity, including lighter intracrystalline regions and partially hollowed domains, which are indicative of selective silicon extraction and the formation of intracrystalline mesoporosity upon desilication, while largely preserving the external crystal morphology (Fig. S1). In contrast, the parent ZSM-5 sample shows a homogeneous contrast consistent with a purely microporous structure. The powder XRD results for desilicated ZSM-5 samples indicated that the overall structure was maintained after desilication (Fig. S2). We attribute the increase in total acid amounts to the increase of the actual aluminum content resulting from silicon dissolution [66,67].

The amorphous silica–alumina catalysts predominantly exhibited weak acidic sites, whereas the zeolite-based catalysts displayed a significantly higher proportion of strong acidic sites (Fig. 3). Among the amorphous silica–alumina catalysts, the catalysts prepared with mixing phase 1 (ASA1 and ASA3) demonstrated a higher total acid content compared to the ones with mixing phase 2 (ASA2 and ASA4). The proposed mechanism for the formation of the acid sites in the amorphous silica–alumina involves the interaction of the surface silanols with nearby aluminum sites, identified as pseudo-bridging silanol groups [68,69]. This interaction requires hydrogen bonding of the silanol group to an external proton receptor, such as tetrahedral (Al(IV)) or pentahedral (Al(V)) coordinated aluminum species. This implies that the coagulation and the hydrolysis of silicon and aluminum species during the catalyst preparation is pivotal for determining not only the total amount, but also the strength of acid sites (Table 1, Fig. 3).

3.2.2. Pyridine-FTIR

To identify the nature of these acid sites, pyridine-FTIR was performed on the four ASA samples. In accordance with the *n*-butylamine titration results, ASA1 and ASA3 exhibited the highest total acidity (Brønsted and Lewis acid sites) after pyridine desorption at 150 °C, with values of 77.8 μmol g^{-1} and 72.0 μmol g^{-1}, respectively (Fig. 4c and d). As previously mentioned, the acidic properties determined by gas-phase probe techniques (such as pyridine-FTIR) do not necessarily correlate quantitatively with liquid-phase titration methods. Therefore, one of the reasons for the higher acid site density measured by potentiometric *n*-butylamine titration is the much stronger basicity of *n*-butylamine compared to pyridine. Because *n*-butylamine is a stronger Brønsted base, it can neutralize very weak acid sites that pyridine may not be able to protonate or interact with strongly enough. In addition, pyridine-FTIR measurements are performed after evacuation at elevated temperatures (150 °C) to remove physisorbed species, resulting in a significantly lower apparent acid concentration. Mass-transfer limitations can be excluded, as the mesoporous structure of ASA (pore size sizes > 100 Å) is

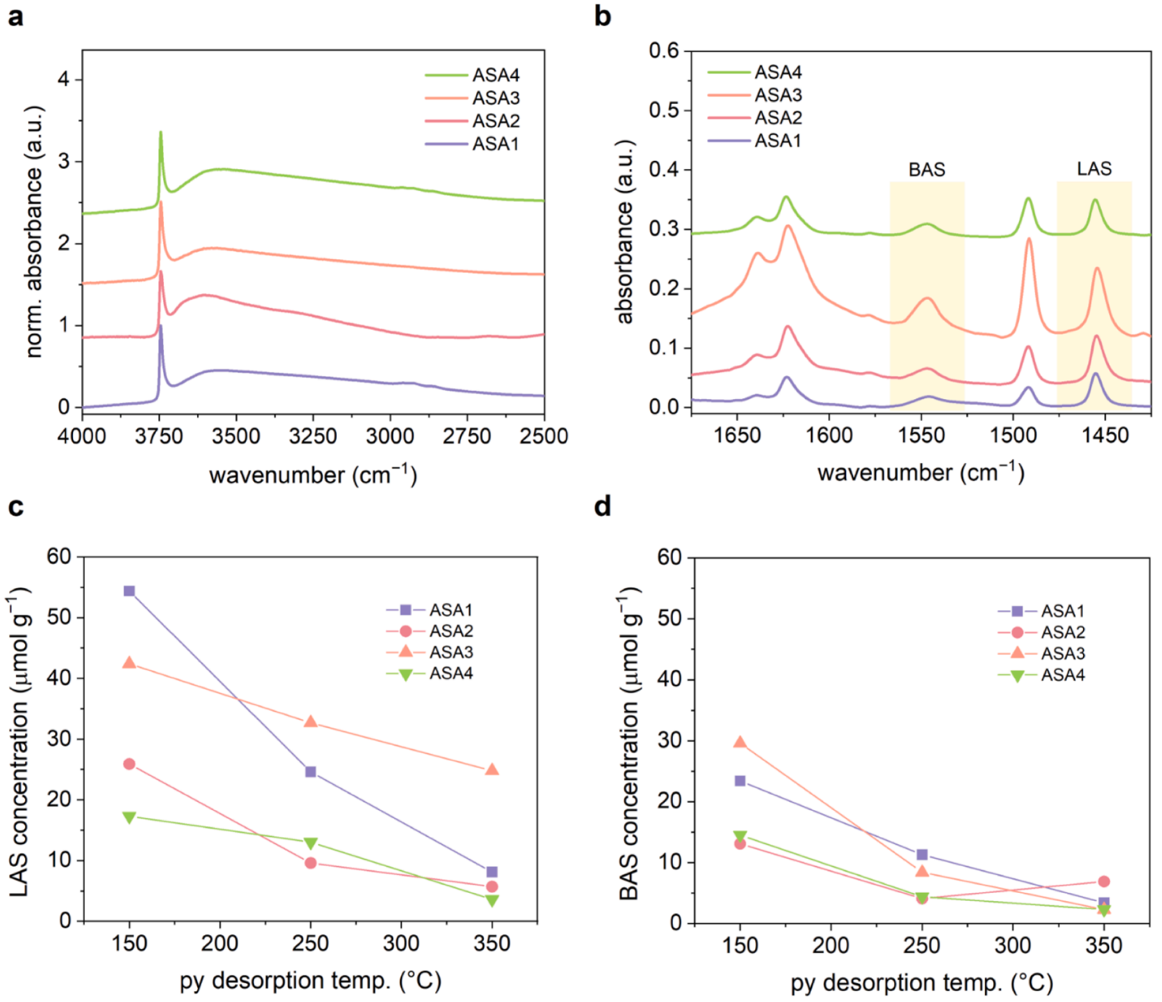

Fig. 4. Acidity of ASA catalysts measured by pyridine FTIR at 150 °C, 250 °C, and 350 °C desorption temperatures. (a) FTIR spectra of the four ASA samples dehydrated under 10^{-6} mbar for 3 h at 450 °C. (b) FTIR spectra zoomed in at the pyridine vibration region. Concentration of Lewis (c) and Brønsted (d) acid sites at different pyridine desorption temperatures.

orders of magnitude larger than the kinetic diameter of pyridine (∼6 Å), ensuring unrestricted access of the probe molecule to internal sites. As expected for amorphous silica–alumina catalysts, all samples showed a higher concentration of Lewis rather than Brønsted acid sites. Upon pyridine desorption at 150 °C, the Brønsted (BAS) to Lewis acid (LAS) sites ratios were found to be 0.4 (ASA1), 0.5 (ASA2), 0.7 (ASA3) and 0.8 (ASA4).

Further insight into the strength of Brønsted (BAS) and Lewis (LAS) acid sites was obtained by pyridine desorption at higher temperatures (Fig. 3c and d). At 150 °C, ASA1 exhibited the highest LAS concentration (54.4 μmol g^{-1}). However, this value decreased sharply with increasing desorption temperature, dropping to 25.9 μmol g^{-1} at 250 °C and to 17.3 μmol g^{-1} at 350 °C (32 % of the initial value), indicating relatively weak LAS. In contrast, ASA3 showed a lower initial LAS concentration at 150 °C (42.4 μmol g^{-1}) but significantly higher thermal stability. Its LAS concentration decreased by only ∼20 % at 250 °C and 350 °C, reaching 24.8 μmol g^{-1} at 350 °C (42 % of the initial value). Consequently, ASA3 retained the highest LAS concentration at the highest desorption temperature, indicating stronger LAS. Regarding BAS, ASA3 showed the highest concentration at 150 °C, but these sites were weaker than those in ASA1, as evidenced by a more pronounced loss at higher desorption temperatures (Fig. 4d).

These results indicate that catalysts prepared using mixing phase 1 exhibit higher total acidity. Along this preparation route, adjusting the pH to 8.7 favors the formation of weaker LAS and stronger BAS, whereas increasing the pH to 9.7 favors the formation of stronger LAS and weaker BAS.

3.3. Catalytic performance

We evaluated the catalytic performance of the prepared catalysts for the isopropylation of naphthalene using gaseous propylene as the isopropylation source (Fig. 5, Fig. S2,S3). Despite the zeolite-based catalysts exhibiting a higher total amount of acid sites, the conversion of naphthalene for these catalysts is low compared to the amorphous silica–alumina catalysts (Fig. 2, Fig. 5a). This suggests the possibility of mass transfer limitations for zeolite-based catalysts [70,71], given that the pore sizes of zeolites typically range from 4 to 8 Å, while the kinetic diameter of naphthalene is approximately 6.5 Å [62,63]. This is further supported by the higher naphthalene conversion of H-Y zeolite (with a pore size of 7.4 Å) compared to MOR (12 MR, 6.5 × 7.0 Å) and the pristine ZSM-5 (5.3 × 5.6 Å), which showed the lowest naphthalene conversion. Additionally, desilication of ZSM-5 via post-treatment was found to be effective in improving naphthalene conversion, likely due to the improved accessibility of acid sites and hierarchical textural properties [72] (Fig. S1).

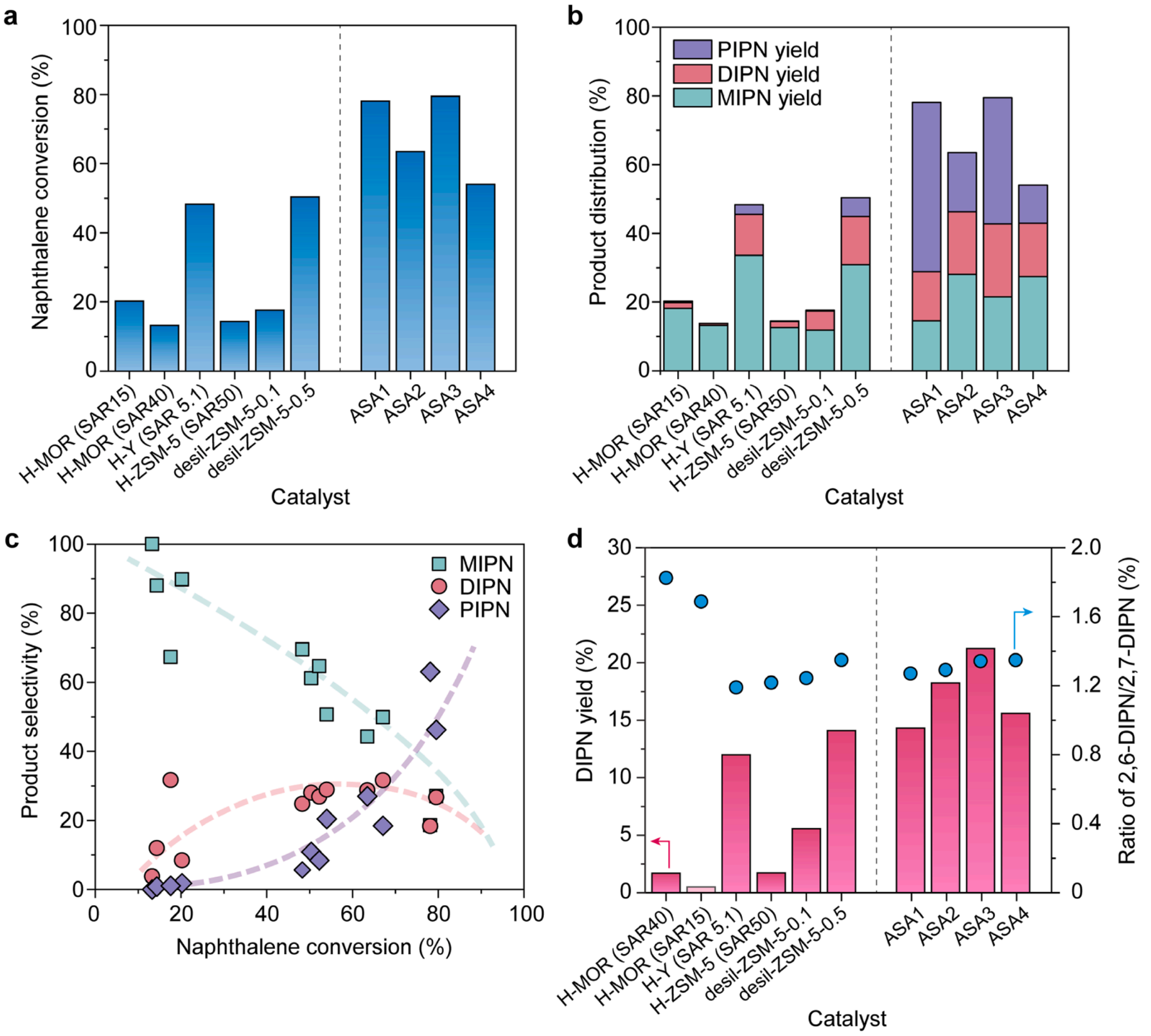

Fig. 5. (a) Conversion of naphthalene. (b) Product distribution of mono-isopropylnaphthalene (MIPN), di-isopropylnaphthalene (DIPN), and tri- and tetra-isopropylnaphthalene (PIPN). (c) Product selectivity plot as a function of naphthalene conversion, calculated from all the prepared catalysts. The dotted lines are added to guide the observed trend. (d) DIPN yield and the selectivity ratio between 2,6-DIPN and 2,7-DIPN.

The amorphous silica–alumina catalysts showed significantly superior catalytic performances in isopropylation of naphthalene (Fig. 5a). We expect that the pore windows larger than 9 nm in the amorphous silica–alumina catalysts can facilitate the access of naphthalene to the acid sites without the mass transfer limitations. These large pores can also accommodate large reactants, such as MIPN and DIPN, facilitating the formation of PIPN in the consecutive reactions (Fig. 1b, Fig. 5b,c). For instance, the amorphous silica–alumina catalysts demonstrated the capability to yield 10–50 % of PIPN, while the reported PIPN yield for H-Y zeolite was below 10 % (Fig. 5b,c) [15]. Among the amorphous silica–alumina catalysts, ASA1 and ASA3 displayed similar naphthalene conversion rates but contrasting product distributions. We expect that, compared to the ASA3, the increased number of strong acid sites of ASA1 contributes to its higher selectivity toward more alkylated products (PIPN), taken together with its larger surface area. In contrast, the ASA3 catalyst exhibited higher selectivity towards DIPN, which can be attributed to the higher content of total weak acid sites (Fig. 2) and weak Brønsted acid sites (Fig. 4d).

In addition to the naphthalene conversion, extensive studies in the literature have investigated the product selectivity of naphthalene isopropylation [12–24,26–28,73–78], which can yield seven different isomers of DIPN (Fig. 1b). The shape-selectivity towards 2,6-DIPN over

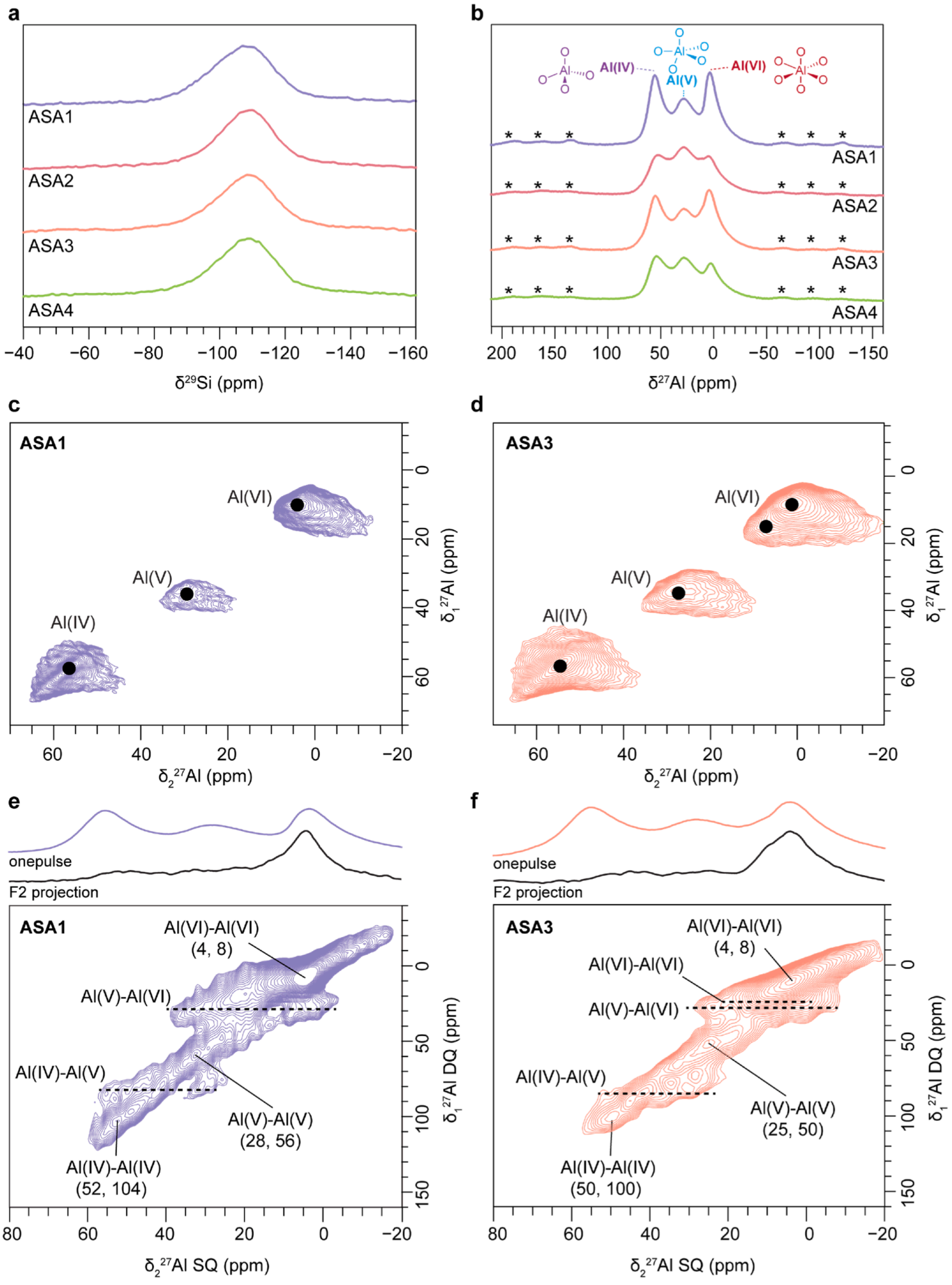

Fig. 6. Solid-state MAS NMR spectra of the prepared amorphous silica–alumina catalysts. (a) 1D ^{29}Si MAS NMR. (b) 1D ^{27}Al MAS NMR. (c, d) 2D ^{27}Al 3Q MAS NMR results for ASA-1 and ASA-3. (e, f) 2D ^{27}Al DQ-SQ results with $BR2_2^1$ recoupling sequence for ASA-1 and ASA-3. All spectra were obtained at the MAS frequency of 20 kHz.

MOR zeolites has been mainly discussed due to its spatial restrictions of the transition states and hindrances during diffusion of the reaction product [16–19,39,73–75]. In other words, MOR zeolites have unique pore structures that specifically facilitate the diffusion of 2,6-DIPN after the reaction, enabling the high selectivity of 2,6-DIPN over 2,7-DIPN [17,39,74,79,80]. We also observed a notable selectivity of 2,6-DIPN over 2,7-DIPN for MOR zeolites (Fig. 4d, Fig. S4). However, despite its higher selectivity toward 2,6-DIPN, it should be highlighted that the overall catalytic performance of MOR zeolites is much lower than that of other catalysts, particularly compared to the amorphous silica–alumina catalysts (Fig. 4a,d). For the amorphous silica–alumina catalysts, the relatively low selectivity for 2,6-DIPN can be addressed by combining with a series of trans-alkylation reactor and vacuum distillation, as outlined in the practical industrial reactor scheme (Fig. 1a).

3.4. *Structural characterization by solid-state NMR*

Due to its amorphous nature, the characterization of the chemical structure of amorphous silica–alumina catalysts is rather limited [43–45]. We used solid-state NMR spectroscopy to gain detailed insights into the structure of the prepared amorphous silica–alumina catalysts (Fig. 6). The ^{29}Si NMR resonances can be assigned to the silicon species as $Q^{4-n}[(4-n-m)\mathrm{Si}, m\mathrm{Al}, n(\mathrm{OH})]$, where n refers to the number of hydroxyl groups and m refers to the number of Al atoms substituting Si atoms at the central silicon atom [81]. The ^{29}Si chemical shifts can be attributed to the silicon species in the amorphous silica–alumina catalysts as the substitutions of silicon atoms by aluminum or OH groups in the first layer, such as Q^4(2Si, 2Al), Q^3(2Si, 1Al, 1OH) and Q^2(2Si, 2OH) at approximately −90 ppm, Q^4(3Si, 1Al) and Q^3(3Si, 1OH) at around −100 ppm, and Q^4(4Si) at around −110 ppm [81–84]. In the series of our amorphous silica–alumina catalysts, the ^{29}Si NMR resonances at −100 and −110 ppm are dominant, while no resonance at −80 ppm was observed (Fig. 6a). As reported in literature, the ^{29}Si NMR resonance at −80 ppm is the evidence of the silanol groups attached to more than one aluminum species [85]. Considering the silicon-to-aluminum ratio of the samples (Si/Al = 6), the ^{29}Si MAS NMR results once again indicate the homogeneous dispersion of Si and Al species in the amorphous silica–alumina catalysts.

The effect of the preparation of amorphous silica–alumina catalysts on the aluminum species was also investigated by ^{27}Al MAS NMR. The ^{27}Al NMR spectra of the amorphous silica–alumina catalysts showed three resonances at ca. 50, 25, and 5 ppm, assigned to tetrahedral (Al(IV)), pentahedral (Al(V)), and octahedral (Al(VI)) aluminum species, respectively (Fig. 5b). It should be noted that, although the aluminum species are well-dispersed in the network of amorphous silicon species (Fig. 2b, Fig. 6a), the coordination of aluminum species are different between the prepared catalysts (Table 1). Similar to the generation of Brønsted acid sites in zeolites due to the replacement of Si by aluminum and the compensation of the consequent charge imbalance by a proton, Al(IV) species incorporated into the amorphous silica network are able to generate BASs on ASA [85–87]. Additionally, the pseudo-bridging silanol group interacting with Al(IV) and Al(V) can behave as Brønsted acid sites and, due to their similar structures, they can show comparable acidity [88]. The Al(IV) and Al(VI) species are well-developed for the amorphous silica–alumina catalysts prepared by mixing phase 1 (ASA1 and ASA3), while the Al(V) species are the major species for the catalysts prepared by mixing phase 2 (ASA2 and ASA4) (Fig. 1, Fig. 6b). Therefore, the distribution of aluminum species are primarily influenced by the mixing phase, and secondarily by the pH adjustment.

Subsequently, we probed the coordination environment of our amorphous silica–alumina catalysts using ^{27}Al triple quantum (3Q) MAS NMR. In the ^{27}Al 3Q MAS spectrum, different Al species can be identified based on their isotopic chemical shifts along F1 dimension, and the variations in the geometry distortions of the aluminum species can be discerned through the quadrupole interactions C_{QCC} (Table 1). Compared to ASA1, the ASA3 catalyst exhibited an additional Al(VI) species at δ_{iso}12.2 ppm (C_{QCC} 4.2 MHz). This observation suggests that, in the coagulation process with reduced nitric acid, the aluminum species tend to coordinate with their environments in octahedral configurations. Furthermore, the penta-coordinated aluminum species in the ASA3 catalyst displayed larger quadrupolar couplings (4.9 MHz) compared to ASA1 (4.0 MHz), suggesting the distortion of Al(V) species in ASA3 induced by the additional Al(VI) species. We infer that the distortion of the Al(V) species in ASA3 induced by the additional Al(VI) species contributes to the higher amount of weak acid sites (Fig.s 3 and 4).

The distribution of aluminum species significantly influences the acid sites in amorphous silica-alumina catalysts [89,90]. We employed 2D ^{27}Al double-quantum single-quantum homonuclear correlation NMR experiment (^{27}Al–^{27}Al DQ–SQ) to analyze the aluminum species distribution (Fig. 5e,f). For ASA1 and ASA3 catalysts, several correlations were observed, including self-correlations of Al(IV), Al(V), and Al(VI), as well as cross-peaks of Al(IV)-Al(V), Al(V)-Al(V), and Al(V)-Al(VI). These correlations in the ^{27}Al–^{27}Al DQ–SQ experiments indicate that different aluminum species are in close proximity, approximately 5 Å [91,92]. Although the local environment of acid sites in amorphous silica–alumina catalysts is still under discussion, pseudo-bridged silanols are considered responsible for acid sites [42,45,46,88–90,93–98], and the presence of aluminum atoms in the silica network enhances the Brønsted acidity of silanols compared to the pristine silica [96]. Silanols bonded to low-coordinated aluminum atoms by a Si-O-Al bridge are proposed as the most acidic Brønsted sites on ASA surfaces, depending on the number and coordination of aluminum atoms [93]. In this regard, we expect that the higher amount of strong acid sites in ASA1 catalyst correlated with the interactions between Al(IV) and Al(V) species in close proximity. On the contrary, for ASA3 catalyst, two different types of Al(VI) species exhibit a rather intense cross-correlation (along the F2 dimension), suggesting their spatial proximity, leading to the formation of weak acid sites. Similarly, the formation of alumina-like clusters (Al (VI) species) in the amorphous silica–alumina catalyst exhibited lower catalytic performance than Al(IV) and Al(V) during the Diels–Alder cycloaddition [99]. The solid-state MAS NMR results thus indicate that the coordination of aluminum species in amorphous silica–alumina catalysts is of relevance for the catalytic performance in naphthalene isopropylation.

Conclusions

In this study, we explored various heterogeneous acidic catalysts, including zeolites and amorphous silica-alumina (ASA), for naphthalene isopropylation. While MOR zeolites exhibit superior shape selectivity towards 2,6-DIPN, their intrinsically low naphthalene conversion rate critically hampers their practical viability in industrial applications. For ASA catalysts, which inherently provide high conversion, we demonstrated that a systematic co-precipitation strategy, specifically controlling the precursor mixing phase and the sequence of pH adjustment, is pivotal in determining the macroscopic acid site distribution and aluminum coordination to control product selectivity. Atomic-scale insights from advanced solid-state NMR revealed that direct mixing at pH 8.7 results in a higher abundance of strong acid sites, attributed to the close proximity of Al(IV) and Al(V) species. While these proximate pairs enable significantly higher naphthalene conversions up to 80 %, they promote silanol groups to strong acid sites that inevitably lead to extensive over-alkylation. Therefore, to precisely control the reaction pathways, when mixing is performed and the pH is subsequently adjusted to 9.7, it yields an ASA catalyst featuring a unique structural motif characterized by two proximal, distinct Al(VI) species. This structural arrangement exhibits stronger Lewis acidity originating from distorted Al(V) species, but its integration within the Al(VI) clustered framework provides a higher density of mild Brønsted acid sites. This tailored weak acidic environment effectively suppresses over-alkylation to favor the selective formation of di-isopropylnaphthalene (DIPN). These findings establish that selective tuning of aluminum coordination through sequence-controlled macroscopic synthesis provides a direct link to the atomic-level structural motifs of acid sites, effectively acting as a catalytic switch to selectively govern aromatic alkylation pathways.

CRediT authorship contribution statement

Sang–Ho Chung: Writing – original draft, Methodology, Investigation, Conceptualization. **José Nuno Almeida:** Investigation, Methodology, Writing – review & editing. **Federico Gubellini:** Methodology, Investigation. **Raghda Makarem:** Investigation, Methodology, Writing – review & editing. **Javier Ruiz–Martínez:** Writing – review & editing, Supervision. **N. Raveendran Shiju:** Writing – review & editing, Supervision, Resources, Project administration, Funding acquisition, Conceptualization.

Declaration of competing interest

The authors declare that they have no known competing financial interests or personal relationships that could have appeared to influence the work reported in this paper.

Acknowledgements

The authors gratefully acknowledge the support of the Dutch Research Council (NWO), RÜTGERS Germany GmbH (currently Rain Carbon), and King Abdullah University of Science and Technology (Saudi Arabia) for funding this work through the Competitive Research Grant URF/1/5083-01-01.

Supplementary materials

Supplementary material associated with this article can be found, in the online version, at doi:10.1016/j.ceja.2026.101137.

Data availability

Data will be made available on request.

References

[1] H.G. Franck, J.W. Stadelhofer, Industrial Aromatic Chemistry, Springer-Verlag Berlin Heidelberg, 1988. Springer-Verlag Berlin Heidelberg.
[2] T. Yang, F.J. Wang, J.P. Huang, S.D. Ling, S.L. Liu, A.G. Zhang, Y.D. Wang, J.H. Xu, Efficient continuous-flow synthesis of long-chain alkylated naphthalene catalyzed by ionic liquids in a microreaction system, React. Chem. Eng. 6 (2021) 1950–1960.
[3] Z.H. Tian, G.L. Zhao, H.M. Jia, B. Li, W.Q. Hu, Preparation of 2,6-diisopropylnaphthalene with recycled process of isomers, Chin. Chem. Lett. 19 (2008) 390–394.
[4] Z.H. Tian, H.M. Jia, G.L. Zhao, W.Q. Hu, Purification of 2,6-diisopropylnaphthalene by static melt crystallization from a mixture containing diisopropylnaphthalene isomers, Chin. J. Chem. 25 (2007) 108–112.
[5] J.C. Mei, Y.Y. Fang, X.Z. Wang, Y.Q. Chen, L.Y. Dai, Phosphorus-/tungsten-doped ZSM-5 composites with a hierarchical structure for efficient production of 2,6-diisopropylnaphthalene, Ind. Eng. Chem. Res. 62 (2023) 10301–10308.
[6] T.H. Lee, H.C. Yu, M. Forrester, T.P. Wang, L.Y. Shen, H.Z. Liu, J.Z. Li, W.Z. Li, G. Kraus, E. Cochran, Next-generation high-performance bio-based naphthalate polymers derived from malic acid for sustainable food packaging, ACS. Sustain. Chem. Eng. 10 (2022) 2624–2633.
[7] L.D. Lillwitz, Production of dimethyl-2,6-naphthalenedicarboxylate: precursor to polyethylene naphthalate, Appl. Catal. a-Gen. 221 (2001) 337–358.
[8] P.J. Hine, A. Astruc, I.M. Ward, Hot compaction of polyethylene naphthalate, J. Appl. Polym. Sci. 93 (2004) 796–802.
[9] C. Bouvier, An Exploration Towards a More Sustainable Process For Dimethyl Naphthalene-2,6-Dicarboxylate Over Acidic Zeolites, Technische Universiteit Delft, 2008.
[10] H.G. Franck, J.W. Stadelhofer, Naphthalene – production and uses, in: H.G. Franck, J.W. Stadelhofer (Eds.), Industrial Aromatic Chemistry: Raw Materials · Processes · Products, Springer Berlin Heidelberg, Berlin, Heidelberg, 1988, pp. 298–333.
[11] C. Subrahmanyam, B. Viswanathan, T.K. Varadarajan, Alkylation of naphthalene with alcohols over acidic mesoporous solids, J. Mol. Catal. A-Chem. 226 (2005) 155–163.
[12] M. Banu, Y.H. Lee, G. Magesh, J.S. Lee, Isopropylation of naphthalene by isopropanol over conventional and Zn- and Fe-modified USY zeolites, Catal. Sci. Technol. 4 (2014) 120–128.
[13] G. Colón, I. Ferino, E. Rombi, E. Selli, L. Forni, P. Magnoux, M. Guisnet, Liquid-phase alkylation of naphthalene by isopropanol over zeolites. Part 1: HY zeolites, Appl. Catal. A 168 (1998) 81–92.
[14] Y. Sugi, Shape-selective alkylation of naphthalene over zeolites: steric interaction of reagents with zeolites, J. Chin. Chem. Soc.-Taip. 57 (2010) 1–13.
[15] C. Bouvier, W. Buijs, J. Gascon, F. Kapteijn, B.C. Gagea, P.A. Jacobs, J.A. Martens, Shape-selective diisopropylation of naphthalene in H-Mordenite: myth or reality? J. Catal. 270 (2010) 60–66.
[16] R. Brzozowski, Isomerization of diisopropylnaphthalenes on wide-pore zeolites, J. Catal. 232 (2005) 366–377.
[17] R. Brzozowski, W. Buijs, Shape-selective synthesis of 2,6-diisopropylnaphthalene on H-mordenite catalysts, J. Catal. 292 (2012) 181–187.
[18] R. Brzozowski, W. Skupinski, Disproportionation of isopropylnaphthalene on zeolite catalysts, J. Catal. 220 (2003) 13–22.
[19] R. Brzozowski, W. Tecza, Shape-selective reactions of naphthalene over zeolites, Appl. Catal. A-Gen. 166 (1998) 21–27.
[20] P. Moreau, A. Finiels, P. Geneste, J. Solofo, Selective isopropylation of naphthalene over zeolites, J. Catal. 136 (1992) 487–492.
[21] P. Moreau, C.Q. He, Z.M. Liu, F. Fajula, Dialkylation of naphthalene with isopropanol over acidic zeolites - influence of pore structure on selectivity, J. Mol. Catal. A-Chem. 168 (2001) 105–114.
[22] D. Mravec, J. Chylik, M. Michvocik, M. Hronec, A. Smieskova, P. Hudec, Isopropylation of naphthalene over dealuminated H-mordenites, Chem. Pap. 52 (1998) 218–221.
[23] Y. Sugi, C. Anand, V.P. Subramaniam, J. Stalin, J.H. Choy, W.S. Cha, A. A. Elzatahry, H. Tamada, K. Komura, A. Vinu, The isopropylation of naphthalene with propene over H-mordenite: the catalysis at the internal and external acid sites, J. Mol. Catal. A-Chem. 395 (2014) 543–552.
[24] Y. Sugi, A. Chakkolingam, S. Joseph, K. Komura, H.G. Jang, S.J. Cho, J.H. Kim, G. Seo, A. Endo, S. Tawada, J. Sonoda, D.M. Aldhayan, A.A. Elzatahry, A. Vinu, Lanthanide oxide modified H-mordenites: deactivation of external acid sites in the isopropylation of naphthalene, Micropor. Mesopor. Mater. 230 (2016) 217–226.
[25] Y. Sugi, X.L. Tu, T. Matsuzaki, T.A. Hanaoka, M. Matsumoto, K. Nakajima, Y. Kubota, J.H. Kim, A. Igarashi, The effect of propylene pressure on shape-selective isopropylation of biphenyl over H-mordenite, Catal. Today 31 (1996) 3–10.
[26] G. Tasi, I. Pálinkó, Comments on “shape-selective diisopropylation of naphthalene in H-mordenite: myth or reality? J. Catal. 279 (2011) 229–230.
[27] H. Yamashita, Y. Mitsukura, H. Kobashi, K. Hiroki, J. Sugiyama, K. Onishi, T. Sakamoto, Microwave-assisted regioselective alkylation of naphthalene compounds using alcohols and zeolite catalysts, Appl. Catal. A-Gen. 381 (2010) 145–149.
[28] A.D. Schmitz, C. Song, Shape-selective isopropylation of naphthalene over dealuminated mordenites. Increasing?-substitution selectivity by adding water, Catal. Lett. 40 (1996) 59–65.
[29] T.C. Keller, J. Arras, M.O. Haus, R. Hauert, A. Kenvin, J. Kenvin, J. Pérez-Ramírez, Synthesis-property-performance relationships of amorphous silica-alumina catalysts for the production of methylenedianiline and higher homologues, J. Catal. 344 (2016) 757–767.
[30] M. Milina, S. Mitchell, N.L. Michels, J. Kenvin, J. Pérez-Ramírez, Interdependence between porosity, acidity, and catalytic performance in hierarchical ZSM-5 zeolites prepared by post-synthetic modification, J. Catal. 308 (2013) 398–407.
[31] R. Cid, G. Pecchi, Potentiometric method for determining the number and relative strength of acid sites in colored catalysts, Appl. Catal. 14 (1985) 15–21.
[32] A.E.R.S. Khder, H.M.A. Hassan, M.S. El-Shall, Acid catalyzed organic transformations by heteropoly tungstophosphoric acid supported on MCM-41, Appl. Catal. A 411-412 (2012) 77–86.
[33] P. Villabrille, P. Vazquez, M. Blanco, C. Caceres, Equilibrium adsorption of molybdosilicic acid solutions on carbon and silica: basic studies for the preparation of ecofriendly acidic catalysts, J. Colloid. Interface Sci. 251 (2002) 151–159.
[34] C.A. Emeis, Determination of integrated molar extinction coefficients for infrared absorption bands of pyridine adsorbed on solid acid catalysts, J. Catal. 141 (1993) 347–354.
[35] Z. Wang, Y. Jiang, F. Jin, C. Stampfl, M. Hunger, A. Baiker, J. Huang, Strongly enhanced acidity and activity of amorphous silica–alumina by formation of pentacoordinated AlV species, J. Catal. 372 (2019) 1–7.
[36] Y. Millot, P.P. Man, Procedures for labeling the high-resolution axis of two-dimensional MQ-MAS NMR spectra of half-integer quadrupole spins, Solid. State Nucl. Magn. Reson. 21 (2002) 21–43.
[37] L. Corti, D. Iuga, J.B. Claridge, M.J. Rosseinsky, F. Blanc, Disorder and oxide ion diffusion mechanism in La(1.54)Sr(0.46)Ga(3)O(7.27) melilite from nuclear magnetic resonance, J. Am. Chem. Soc. 145 (2023) 21817–21831.
[38] Q. Wang, W. Li, I. Hung, F. Mentink-Vigier, X. Wang, G. Qi, X. Wang, Z. Gan, J. Xu, F. Deng, Mapping the oxygen structure of gamma-Al(2)O(3) by high-field solid-state NMR spectroscopy, Nat. Commun. 11 (2020) 3620.
[39] R. Brzozowski, W. Skupinski, M.H. Jamroz, M. Skarzynski, H. Otwinowska, Isolation and identification of diisopropylnaphthalene isomers in the alkylation products of naphthalene, J. Chromatogr. A 946 (2002) 221–227.
[40] A. Ishihara, Preparation of amorphous silica-alumina using the sol-gel method and its reactivity for a matrix in catalytic cracking, Catal. Surv. Asia 16 (2012) 36–47.
[41] A. Ishihara, H. Negura, T. Hashimoto, H. Nasu, Catalytic properties of amorphous silica-alumina prepared using malic acid as a matrix in catalytic cracking of n-dodecane, Appl. Catal. a-Gen. 388 (2010) 68–76.

[42] J. Bao, Q.H. Yang, S.Q. Zeng, X.Y. Sang, W.M. Zhai, H. Nie, Synthesis of amorphous silica-alumina with enhanced specific surface area and acidity by pH-swing method and its catalytic activity in cumene cracking, Micropor. Mesopor. Mater. 337 (2022) 111897.
[43] F. Leydier, C. Chizallet, A. Chaumonnot, M. Digne, E. Soyer, A.A. Quoineaud, D. Costa, P. Raybaud, Bronsted acidity of amorphous silica-alumina: the molecular rules of proton transfer, J. Catal. 284 (2011) 215–229.
[44] F. Leydier, C. Chizallet, D. Costa, P. Raybaud, CO adsorption on amorphous silica-alumina: electrostatic or Bronsted acidity probe? Chem. Commun 48 (2012) 4076–4078.
[45] F. Leydier, C. Chizallet, D. Costa, P. Raybaud, Revisiting carbenium chemistry on amorphous silica-alumina: unraveling their milder acidity as compared to zeolites, J. Catal. 325 (2015) 35–47.
[46] D. Yun, Y.S. Yun, T.Y. Kim, H. Park, J.M. Lee, J.W. Han, J. Yi, Mechanistic study of glycerol dehydration on Bronsted acidic amorphous aluminosilicate, J. Catal. 341 (2016) 33–43.
[47] Z. Wang, K. Chen, Y. Jiang, J. Trebosc, W. Yang, J.P. Amoureux, I. Hung, Z. Gan, A. Baiker, O. Lafon, J. Huang, Revealing bronsted acidic bridging SiOHAl groups on amorphous silica-alumina by ultrahigh field solid-State NMR, J. Phys. Chem. Lett. 12 (2021) 11563–11572.
[48] S.H. Chung, J.C.N. de Miguel, T. Li, P. Lavrik, S. Komaty, Y. Yuan, D. Poloneeva, W. H. Anbari, M.N. Hedhili, M. Zaarour, C. Martín, T. Shoinkhorova, E. Abou–Hamad, J. Gascon, J. Ruiz–Martínez, Core–shell structured magnesia–silica as a next generation catalyst for one-step ethanol-to-butadiene Lebedev process, Appl. Catal. B: Environ. Energy 344 (2024) 123628.
[49] A. Khanna, D.G. Bhat, Nanocrystalline gamma alumina coatings by inverted cylindrical magnetron sputtering, Surf. Coat Tech. 201 (2006) 168–173.
[50] L. Samain, A. Jaworski, M. Edén, D.M. Ladd, D.K. Seo, F. Javier Garcia-Garcia, U. Häussermann, Structural analysis of highly porous γ-Al2O3, J. Solid. State Chem. 217 (2014) 1–8.
[51] R. Snel, Control of the porous structure of amorphous silica-alumina, Appl. Catal. 11 (1984) 271–280.
[52] V.G. Baldovino-Medrano, V. Niño-Celis, R.I. Giraldo, Systematic analysis of the nitrogen adsorption-desorption isotherms recorded for a series of materials based on microporous-mesoporous amorphous aluminosilicates using classical methods, J. Chem. Eng. Data 68 (2023) 2512–2528.
[53] M. Thommes, K. Kaneko, A.V. Neimark, J.P. Olivier, F. Rodriguez-Reinoso, J. Rouquerol, K.S.W. Sing, Physisorption of gases, with special reference to the evaluation of surface area and pore size distribution (IUPAC Technical Report), Pure Appl. Chem. 87 (2015) 1051–1069.
[54] L. Rodríguez-González, F. Hermes, M. Bertmer, E. Rodríguez-Castellón, A. Jiménez-López, U. Simon, The acid properties of H-ZSM-5 as studied by NH3-TPD and 27Al-MAS-NMR spectroscopy, Appl. Catal. A 328 (2007) 174–182.
[55] N. Batalha, S. Morisset, L. Pinard, I. Maupin, J.L. Lemberton, F. Lemos, Y. Pouilloux, BEA zeolite nanocrystals dispersed over alumina for -hexadecane hydroisomerization, Micropor. Mesopor. Mater. 166 (2013) 161–166.
[56] F. Jin, Y.D. Li, A FTIR and TPD examination of the distributive properties of acid sites on ZSM-5 zeolite with pyridine as a probe molecule, Catal. Today 145 (2009) 101–107.
[57] K. Yu, N. Kumar, A. Aho, J. Roine, I. Heinmaa, D.Y. Murzin, A. Ivaska, Determination of acid sites in porous aluminosilicate solid catalysts for aqueous phase reactions using potentiometric titration method, J. Catal. 335 (2016) 117–124.
[58] L. Pizzio, P. Vázquez, C. Cáceres, M. Blanco, Tungstophosphoric and molybdophosphoric acids supported on zirconia as esterification catalysts, Catal Lett. 77 (2001) 233–239.
[59] J. Pastvova, D. Kaucky, J. Moravkova, J. Rathousky, S. Sklenak, M. Vorokhta, L. Brabec, R. Pilar, I. Jakubec, E. Tabor, P. Klein, P. Sazama, Effect of enhanced accessibility of acid sites in micromesoporous mordenite zeolites on hydroisomerization of -hexane, ACS. Catal. 7 (2017) 5781–5795.
[60] A. Bolshakov, D.E.R. Hidalgo, A.J.F. van Hoof, N. Kosinov, E.J.M. Hensen, Mordenite nanorods prepared by an inexpensive pyrrolidine-based mesoporogen for alkane hydroisomerization, ChemCatChem 11 (2019) 2803–2811.
[61] L. Shirazi, E. Jamshidi, M.R. Ghasemi, The effect of Si/Al ratio of ZSM-5 zeolite on its morphology, acidity and crystal size, Cryst. Res. Technol. 43 (2008) 1300–1306.
[62] W.M. Hao, W.M. Zhang, Z.B. Guo, J.H. Ma, R.F. Li, Mesoporous beta zeolite catalysts for benzylation of naphthalene: effect of pore structure and acidity, Catalysts 8 (2018), 504-504.
[63] Z.Y. Li, Y.S. Liu, X. Yang, Y. Xing, Z.Y. Wang, Q. Yang, R.T. Yang, Desorption kinetics of naphthalene and acenaphthene over two activated carbons via thermogravimetric analysis, Energy Fuels. 29 (2015) 5303–5310.
[64] J.J. Liu, H.F. Zhang, N.Y. Lu, X.L. Yan, B.B. Fan, R.F. Li, Influence of acidity of mesoporous ZSM-5-supported Pt on naphthalene hydrogenation, Ind. Eng. Chem. Res. 59 (2020) 1056–1064.
[65] Y.C. Wang, O.V. Kikhtyanin, C. Li, X.F. Su, X.F. Bai, W. Wu, Synthesis of nanosized ZSM-5 zeolites by different methods and their catalytic performance in the alkylation of naphthalene, Pet. Chem+ 61 (2021) 394–406.
[66] M. Milina, S. Mitchell, N.L. Michels, J. Kenvin, J. Pérez-Ramírez, Interdependence between porosity, acidity, and catalytic performance in hierarchical ZSM-5 zeolites prepared by post-synthetic modification, J. Catal. 308 (2013) 398–407.
[67] K.A. Tarach, K. Góra-Marek, J. Martinez-Triguero, I. Melián-Cabrera, Acidity and accessibility studies of desilicated ZSM-5 zeolites in terms of their effectiveness as catalysts in acid-catalyzed cracking processes, Catal. Sci. Technol. 7 (2017) 858–873.
[68] E.J.M. Hensen, D.G. Poduval, V. Degirmenci, D.A.J.M. Ligthart, W. Chen, F. Maugé, M.S. Rigutto, J.A.R.V. Veen, Acidity characterization of amorphous Silica–Alumina, J. Phys. Chem. C 116 (2012) 21416–21429.
[69] F. Leydier, C. Chizallet, D. Costa, P. Raybaud, CO adsorption on amorphous silica–alumina: electrostatic or Brønsted acidity probe? Chem. Commun. 48 (2012) 4076–4078.
[70] P. Peng, D. Stosic, X.M. Liu, Z.F. Yan, S. Mintova, Strategy towards enhanced performance of zeolite catalysts: raising effective diffusion coefficient versus reducing diffusion length, Chem. Eng. J. 385 (2020) 123800.
[71] P. Peng, X.H. Gao, Z.F. Yan, S. Mintova, Diffusion and catalyst efficiency in hierarchical zeolite catalysts, Natl. Sci. Rev. 7 (2020) 1726–1742.
[72] N.J. Venkatesha, Y.S. Bhat, B.S.J. Prakash, Dealuminated BEA zeolite for selective synthesis of five-membered cyclic acetal from glycerol under ambient conditions, RSC. Adv. 6 (2016) 18824–18833.
[73] R. Brzozowski, Polemic against conclusions drawn in “shape-selective diisopropylation of naphthalene in H-Mordenite: myth or reality?” (J. Catal., 270 (2010) 60–66), J. Catal. 280 (2011) 137–141.
[74] R. Brzozowski, W. Skupinski, Zeolite pore entrance effect on shape selectivity in naphthalene isopropylation, J. Catal. 210 (2002) 313–318.
[75] W. Buijs, P.A. Jacobs, J.A. Martens, Reply to the letter of Robert Brzozowski concerning the conclusions drawn in “shape-selective diisopropylation of naphthalene in H-Mordenite: myth or reality? J. Catal. 280 (2011) 142–143.
[76] S.J. Chu, Y.W. Chen, Isopropylation of naphthalene over beta-zeolite, Ind. Eng. Chem. Res. 33 (1994) 3112–3117.
[77] J.H. Kim, Y. Sugi, T. Matsuzaki, T. Hanaoka, Y. Kubota, X. Tu, M. Matsumoto, Effect of Sio2al2o3 ratio of H-Mordenite on the isopropylation of naphthalene with propylene, Micropor. Mater. 5 (1995) 113–121.
[78] J. Wang, J.N. Park, Y.K. Park, C.W. Lee, Isopropylation of naphthalene by isopropyl alcohol over USY catalyst: an investigation in the high-pressure fixed-bed flow reactor, J. Catal. 220 (2003) 265–272.
[79] A. Katayama, M. Toba, G. Takeuchi, F. Mizukami, S. Niwa, S. Mitamura, Shape-selective synthesis of 2,6-diisopropylnaphthalene over H-Mordenite catalyst, J. Chem. Soc. Chem. Comm. (1991) 39–40.
[80] R. Millini, F. Frigerio, G. Bellussi, G. Pazzuconi, C. Perego, P. Pollesel, U. Romano, A priori selection of shape-selective zeolite catalysts for the synthesis of 2,6-dimethylnaphthalene, J. Catal. 217 (2003) 298–309.
[81] P.P. Man, M.J. Peltre, D. Barthomeuf, Nuclear-magnetic-resonance study of the dealumination of an amorphous silica-alumina catalyst, J. Chem. Soc. Faraday T 86 (1990) 1599–1602.
[82] A.G.M. Rankin, P.B. Webb, D.M. Dawson, J. Viger-Gravel, B.J. Walder, L. Emsley, S.E. Ashbrook, Determining the surface structure of silicated alumina catalysts via isotopic enrichment and dynamic nuclear polarization surface-enhanced NMR spectroscopy, J. Phys. Chem. C. Nanomater. Interfac. 121 (2017) 22977–22984.
[83] Z. Wang, R. Buechel, Y. Jiang, L. Wang, H. Xu, P. Castignolles, M. Gaborieau, O. Lafon, J.P. Amoureux, M. Hunger, A. Baiker, J. Huang, Engineering the distinct structure interface of subnano-alumina domains on silica for acidic amorphous silica-alumina toward biorefining, JACS. Au 1 (2021) 262–271.
[84] T. Li, L. Zhang, Z.C. Tao, C.X. Hu, C.L. Zhao, F.J. Yi, X. Gao, X.D. Wen, Y. Yang, Y. W. Li, Synthesis and characterization of amorphous silica-alumina with enhanced acidity and its application in hydro-isomerization/cracking, Fuel 279 (2020) 118487.
[85] J. Huang, N. van Vegten, Y. Jiang, M. Hunger, A. Baiker, Increasing the Bronsted acidity of flame-derived silica/alumina up to zeolitic strength, Angew. Chem. Int. Ed. Engl. 49 (2010) 7776–7781.
[86] Q. Luo, F. Deng, Z. Yuan, J. Yang, M. Zhang, Y. Yue, C. Ye, Using trimethylphosphine as a probe molecule to study the acid sites in Al—MCM-41 materials by solid-State NMR spectroscopy, J. Phys. Chem. B 107 (2002) 2435–2442.
[87] Z.C. Wang, Y.J. Jiang, R. Rachwalik, Z.W. Liu, J. Shi, M. Hunger, J. Huang, One-step room-temperature synthesis of [Al]MCM-41 materials for the catalytic conversion of phenylglyoxal to ethylmandelate, ChemCatChem 5 (2013) 3889–3896.
[88] Z. Wang, Y. Jiang, O. Lafon, J. Trebosc, K. Duk Kim, C. Stampfl, A. Baiker, J. P. Amoureux, J. Huang, Bronsted acid sites based on penta-coordinated aluminum species, Nat. Commun. 7 (2016) 13820.
[89] F.A. Perras, Z. Wang, T. Kobayashi, A. Baiker, J. Huang, M. Pruski, Shedding light on the atomic-scale structure of amorphous silica-alumina and its Bronsted acid sites, Phys. Chem. Chem. Phys. 21 (2019) 19529–19537.
[90] Z. Wang, T. Li, Y. Jiang, O. Lafon, Z. Liu, J. Trebosc, A. Baiker, J.P. Amoureux, J. Huang, Acidity enhancement through synergy of penta- and tetra-coordinated aluminum species in amorphous silica networks, Nat. Commun. 11 (2020) 225.
[91] S.H. Chung, T. Li, T. Shoinkhorova, S. Komaty, A. Ramirez, I. Mukhambetov, E. Abou-Hamad, G. Shterk, S. Telalovic, A. Dikhtiarenko, B. Sirks, P. Lavrik, X. Tang, B.M. Weckhuysen, P.C.A. Bruijnicx, J. Gascon, J. Ruiz-Martínez, Origin of active sites on silica–magnesia catalysts and control of reactive environment in the one-step ethanol-to-butadiene process, Nat. Catal. 6 (2023) 363–376.
[92] J. Brus, J. Czernek, M. Urbanova, L. Kobera, A. Jegorov, An efficient 2D (11)B-(11) B solid-state NMR spectroscopy strategy for monitoring covalent self-assembly of boronic acid-derived compounds: the transformation and unique architecture of bortezomib molecules in the solid state, Phys. Chem. Chem. Phys. 19 (2016) 487–495.
[93] C. Chizallet, P. Raybaud, Acidity of amorphous silica-alumina: from coordination promotion of Lewis sites to proton transfer, Chemphyschem 11 (2010) 105–108.
[94] G. Crepeau, V. Montouillout, A. Vimont, L. Mariey, T. Cseri, F. Mauge, Nature, structure and strength of the acidic sites of amorphous silica alumina: an IR and NMR study, J. Phys. Chem. B 110 (2006) 15172–15185.

[95] E.J.M. Hensen, D.G. Poduval, V. Degirmenci, D.A.J.M. Ligthart, W.B. Chen, F. Maugé, M.S. Rigutto, J.A.R. van Veen, Acidity characterization of amorphous silica-alumina, J. Phys. Chem. C 116 (2012) 21416–21429.

[96] F. Leydier, C. Chizallet, A. Chaumonnot, M. Digne, E. Soyer, A.A. Quoineaud, D. Costa, P. Raybaud, Brønsted acidity of amorphous silica–alumina: the molecular rules of proton transfer, J. Catal. 284 (2011) 215–229.

[97] A.R. Mouat, T. Kobayashi, M. Pruski, T.J. Marks, P.C. Stair, Direct spectroscopic evidence for isolated silanols in SiOx/Al2O3 and their formation mechanism, J. Phys. Chem. C 121 (2017) 6060–6064.

[98] W.S. Salvia, T.Y. Zhao, P. Chatterjee, W. Huang, F.A. Perras, Are the Brønsted acid sites in amorphous silica–alumina bridging? Chem. Commun. 59 (2023) 13962–13965.

[99] F.J.A.G. Coumans, E. Demiröz, N. Kosinov, E.J.M. Hensen, Amorphous silica-alumina as suitable catalyst for the diels-alder cycloaddition of dimethylfuran and ethylene to biobased xylene, ChemCatChem 14 (2022) e202200266.